Multimodal analysis and comparison of stoichiometric and structural characteristics of parosteal and conventional osteosarcoma with massive sclerosis in human bone

Benjamin Zanghellini, Nicole Zechmann, Dieter Baurecht, Tilman A Grünewald, Manfred Burghammer, Bernadette Liegl-Atzwanger, Andreas Leithner, Anton Davydok, Helga Lichtenegger

Journal of Structural Biology 216 (2024) 108106

Contents lists available at ScienceDirect

Journal of Structural Biology

journal homepage: www.elsevier.com/locate/yjsbi

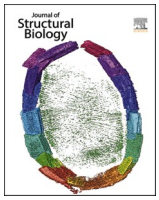

Research Article

Multimodal analysis and comparison of stoichiometric and structural characteristics of parosteal and conventional osteosarcoma with massive sclerosis in human bone

Benjamin Zanghellini [a], Nicole Zechmann [b], Dieter Baurecht [c], Tilman A. Grünewald [d], Manfred Burghammer [e], Bernadette Liegl-Atzwanger [f], Andreas Leithner [b], Anton Davydok [g], Helga Lichtenegger [a,*]

[a] Institute of Physics and Material Science, BOKU University, Vienna, Austria
[b] Department of Orthopedics and Trauma, Medical University of Graz, Austria
[c] Institute of Physical Chemistry, University of Vienna, Austria
[d] Aix Marseille Univ, CNRS, Centrale Med, Institut Fresnel, Marseille, France
[e] The European Synchrotron, Grenoble, France
[f] Institute of Pathology, Medical University of Graz, Austria
[g] Institute of Materials Physics, Helmholtz Zentrum Hereon, Hamburg, Germany

ARTICLE INFO

Edited by Elia Beniash

Keywords:
Bone
Osteosarcoma
Crystal structure
Carbonate substitution
Raman spectroscopy
X-ray diffraction

ABSTRACT

Osteosarcoma (OS) is the most common malignant primary bone tumor in humans and occurs in various subtypes. Tumor formation happens through malignant osteoblasts producing immature bone. In the present paper we studied two different subtypes of osteosarcoma, from one individual with conventional OS with massive sclerosis and one individual with parosteal OS, based on a multimodal approach including small angle x-ray scattering (SAXS), wide angle x-ray diffraction (WAXS), backscattered electron imaging (BEI) and Raman spectroscopy. It was found that both tumors showed reduced mineral particle sizes and degree of orientation of the collagen-mineral composite in the affected areas, alongside with a decreased crystallinity. Distinct differences between the tumor material from the two individuals were found in the degree of mineralization. Further differences were observed in the carbonate to phosphate ratio, which is related to the degree of carbonate substitution in bone mineral and indicative of the turnover rate. The contraction of the c-axis of the bone mineral crystals proved to be a further, very sensitive parameter, potentially indicative of malignancy.

1. Introduction

Osteosarcoma (OS) is a primary malignant bone tumor (Baumhoer, 2018; Tobias and Hochhauser, 2015). The exact origin of osteosarcoma cells is still not completely understood. Osteoblastic cells of the mesenchymal tumor produce defective osteoid, a soft and non-mineralized basic substance of bone tissue, which further matures into tumorous bone tissue (Kansara and Thomas, 2007; Lokau, 2020). According to the recent WHO Classification Soft Tissue and Bone Tumors 2020, OS can be divided in 4 major categories: (1) conventional high-grade OS and its histologic subtypes, (2) surface OS, (3) high grade secondary OS arising in diseased bone and (4) intramedullary well differentiated OS.

Healthy bone is a hierarchical structured material on different length scales (Dorozhkin and Epple, 2002). These levels of organization can be differentiated into macrostructure, micro- and sub-microstructure, nano- and sub-nanostructure (Rho et al., 1998). At nanoscale level, each individual collagen fiber consists of fibrils, which in turn is an assembly of collagen molecules forming the framework into which the mineral is deposited (Launey et al., 2010). The organic matrix is represented to 90–95 % by the type-I collagen (Mottaghitalab et al., 2015; Posner, 1969). The mineral crystal, primarily consisting of hydroxyapatite ($Ca_{10}(PO_4)_6(OH)_2$), is the main inorganic material which grows into/onto the organic matrix (Lowenstam and Weiner, 1989; Watson and Avery, 1954; Weiner and Wagner, 1998). With the advance of new analytical methods, this picture has seen significant refinement in recent

* Corresponding author.
E-mail address: helga.lichtenegger@boku.ac.at (H. Lichtenegger).

https://doi.org/10.1016/j.jsb.2024.108106
Received 28 November 2023; Received in revised form 10 June 2024; Accepted 10 June 2024
Available online 12 June 2024

years. It is understood now that the bone mineral is organized in an extensive inter- and extrafibrillar mineral network (Grandfield et al., 2018; Reznikov et al., 2014; Reznikov et al., 2018; Schwarcz et al., 2014). Further, x-ray tensor tomography experiments could show that a localized orientation difference between the mineral fraction and the associated nanostructure exists (Grünewald et al., 2020) and a more in-depth analysis of bone mineral properties with x-ray diffraction tomography shows strong local variations, most likely stemming from varying chemical conditions during growth (Wittig et al., 2019). This notion of chemical complexity in the hydroxyapatite mineral structure is also reflected by NMR studies which underlined the stabilizing role of ions and small molecules during mineral formation (Wang et al., 2013) and subsequent assembly of the crystallites (Davies et al., 2014). All these new information led to a more refined understanding of the bone formation. Bone mineralization has been suggested to be based on a stenciling principle, that is the localized activation of mineralization by enzymatic degradation of growth inhibitors in the extracellular matrix (McKee et al., 2022; Reznikov et al., 2020). A comprehensive review of the hierarchical structure of bone is for example given by Rodriguez-Palomo (Rodriguez-Palomo et al., 2023).

Compared to synthetic hydroxyapatite (HAp), the human bone mineral differs in composition due to additional ions that are substituted: mainly CO_3^{-2} ions substituting in the hydroxyapatite lattice either for the PO_4^{-3} (B-type carbonated apatite) or the OH^- (A-type carbonated apatite) ions (Madupalli et al., 2017; Posner, 1969). Thus, changes in the a- and c-axes of the apatite lattice are manifested due to the substitution site of the ions (LeGeros et al., 1969).

Small-angle x-ray scattering (SAXS) and wide-angle x-ray scattering (WAXS) are powerful methods to study hierarchically structured biological materials including bone. The SAXS signal in bone mainly arises from the electron density contrast on the nanometer scale between collagen fibers and mineral. SAXS has been used for example to characterize the size of mineral particles in bone, by evaluating the so-called T parameter, which corresponds to a typical distance of different phases (collagen and mineral) in the sample (Fratzl, 1994; Pabisch et al., 2013). Furthermore, the SAXS signal can be used to study the preferred orientation of the collagen and mineral composite, which is typically along the long axis in the corticalis of long bones or along trabeculae in spongy bone (Karunaratne et al., 2012; Rinnerthaler et al., 1999). These structural parameters are indicative of bone quality and have been found to change for example close to implants or in tumorous tissue (Grünewald et al., 2016a; Zanghellini et al., 2019). Crystallographic information on the bone mineral HAp can be obtained from WAXS. Changes in the lattice spacing or the crystallinity are readily identified and may occur upon ion substitution (Cheng et al., 2019; Grünewald et al., 2016b; Lala et al., 2016). Furthermore, alterations of the lattice spacing of HAp can be caused by mechanical deformation, see e.g. (Almer and Stock, 2005) on residual strain, or by the interaction of mineral with the collagen phase (Gupta et al., 2006; Wang and Gupta, 2011).

Backscattered electron imaging (BEI) is a very useful technique to map the mineral density in bone samples. It is carried out in a scanning electron microscope (SEM) and relies on the dependence of the probability of electron backscattering events on the atomic number Z of elements in the sample volume probed by the electron beam. Roschger et al. have pioneered the use of BEI on bone in a semi-quantitative way, by using standard materials to determine the local Ca concentration from the intensity contrast (Roschger et al., 1998). This approach has also been used to study mineralization differences in healthy bone and sclerosing osteosarcoma (Hofstaetter et al., 2013; Zanghellini et al., 2019).

Raman spectroscopy is based on the interaction between light and matter to provide details of the chemical composition and structure on a molecular level in tissues. Compared to other methods its nondestructive applicability to fresh hydrated tissue is advantageous (Morris and Mandair, 2011). This technology was used in several studies to analyze changes in bone due to diseases and can be a future tool for early diagnostics (McCreadie et al., 2006; Morris and Mandair, 2011). It was for example used in experiments to investigate the mineralization in osteoporosis (Kim et al., 2014), detect the effect of osteogenesis imperfecta (Imbert et al., 2014) or osteomyelitis (Khalid et al., 2018) on bone. Several studies used this method to measure changes in the composition of bone and alterations of the mineral when affected by prostate or breast metastases in humans (Bi et al., 2010) or mice (Bi et al., 2013; Ding et al., 2014; He et al., 2017).

Nevertheless, it is not fully understood how different osteosarcoma types affect the bone composition and whether structural bone changes or stoichiometric mineral changes are tumor-type dependent or a general phenomenon of any type of OS. Previous studies analyzed often only bone metastases on different levels.

In this manuscript we present a multimodal approach to analyze changes in bone due to a primary bone tumor and were for the first time able to compare ultrastructure and mineralization of osteosarcoma material of two different types from two individuals. For this purpose, we combine Raman spectroscopy, electron microscopy and x-ray scattering on a parosteal OS and relate the results to Raman data from a sclerosing OS, together with previously obtained structural data on the sclerosing OS sample (Zanghellini et al., 2019). We find an altered mineral crystallinity, pronounced changes in the orientation and thickness of mineral platelets, and tumor-related stoichiometric changes in the bone mineral. These findings might be useful in future early diagnostics.

2. Materials & methods

2.1. Bone samples and sample preparation

Human bone samples were collected from a male and a female patient after surgical resections, suffering from a conventional OS with massive scleroses and a parosteal osteosarcoma, respectively. The specimens were divided in different parts, referring to their pathological characteristics and are classified as sclerosing osteosarcoma normal bone areas (N_s), sclerosing osteosarcoma tumorous bone areas (T_s), parosteal osteosarcoma normal bone areas (N_p) and parosteal osteosarcoma tumorous bone areas (T_p). Since the sclerosing OS grew inside normal trabecular bone, tumorous and normal bone were located in the same sample. By contrast, the parosteal OS arises from the outer layer of the periosteum and grows at the bone surface. Therefore, the tumorous tissue was separate from normal bone and both were analyzed as individual pieces. All formalin-fixed samples were embedded in polymethylmethacrylate resin (Technovit® 9100), afterwards slices (thickness 200–250 μm) were produced on an Accutom-50 diamond saw from Struers. These samples then were first used for small-angle and wide-angle x-ray scattering measurements (SAXS/WAXS). Afterwards, the thin slices were fixed on a sample holder by a two-component glue and further ground and polished wet in several steps (grain sizes were decreased from 500 to 4000 in 4 steps, the polishing process was based on the usage of an alpha alumina suspension). After preparation, backscattered electron imaging (BEI) and Raman measurements were carried out.

2.2. Small-angle and wide-angle x-ray scattering

SAXS/WAXS measurements were performed at the synchrotron radiation facilities ESRF/ID13 (Avenue des Martyrs, 38000 Grenoble, France) and at PETRAIII/P03 (DESY, Notkestrasse, 22607 Hamburg, Germany). A detailed description of the ESRF/ID 13 experimental setup, where the sclerosing OS was already analyzed by SAXS/WAXS can be found in (Zanghellini et al., 2019). The same setup at ESRF/ID13 was used for SAXS on parosteal OS. In brief, a focused x-ray beam of 1.3 × 2.5 μm (v × h) size at 13 keV photon energy was used. Free-standing, dry bone slices containing either normal or tumorous bone were scanned using a continuous scanning scheme with a horizontal step size of 10 μm

and a vertical step size of 10 μm. Diffraction patterns were collected at 5 ms exposure time using an Eiger 4 M detector at a sample-detector distance of 173 mm (calibrated by an Al_2O_3 standard (NIST SRM 674b)). The instrumental resolution of the ESRF experiment was estimated as 1.95 mrad by evaluating the data from the Al_2O_3 standard measurement via a Rietveld refinement. This translates into a d spacing resolution of 0.0024 nm for the 002 reflection in HAp.

WAXS measurements of parosteal OS specimen were carried out at PETRAIII/P03. The same free-standing bone sections as used for SAXS at ESRF/ID13 were mounted on a sample holder and placed in the beam path. The beam diameter was 300 nm, the incident beam had an energy of 13 keV and the sample distance was 255 mm (calibrated by the use of LaB_6 (NIST SRM 660c)). Data were collected in 10 μm steps and with an exposure time of 2 s per data point. For both bone tissue types (tumorous and normal bone) area sizes of 500 × 200 μm were measured at two different locations each.

Datasets were acquired with an Eiger 9 M detector. The instrumental resolution was determined by evaluating data from the LaB_6 standard with Rietveld refinement, which yielded a resolution of 2.07 mrad, corresponding to a d spacing resolution of 0.0026 nm for the 002 reflection in HAp, very similar to the experiment at ESRF/ID13.

Data were integrated in pyFAI and evaluated with self-written Python routines. The first step of data treatment (radial and azimuthal SAXS data integration) delivers curves displaying the intensity as function of azimuth χ or the scattering vector q. Evaluation of these curves gives insights in the bone characteristics concerning thickness and degree of orientation of mineral particles through the so-called T-parameter and ρ-parameter, respectively (Fratzl et al., 1996; Fratzl et al., 1991; Pabisch et al., 2013). Details about the SAXS data evaluation can be found in (Zanghellini et al., 2019).

The azimuthal data integration of the intensity of the WAXS signal allows to analyze the c-axis of the hydroxyapatite crystals (HAp) in bone by calculating the d-spacing of the 002 reflection:

$$d_{hkl} = \frac{2\pi}{q} \text{and } d_{hkl} = \frac{4}{3}\left(\frac{h^2 + hk + k^2}{a^2}\right) + \frac{l^2}{c^2}$$

where q is the scattering vector, h, k, and l are representing the Miller indices and a and c are the crystals unit cell axes in a hexagonal crystal.

2.3. Backscattered electron imaging

Backscattered electron imaging (BEI) was performed on a scanning electron microscope (Quanta 250 FEG, company FEI) at the University of Natural Resources and Life Sciences, Austria. To enable a conductive surface and avoid any charges on the sample, all specimens were sputtered with a thin gold layer. In all measurements, the beam energy was kept at 20 kV and the working distance was set at 10 mm. This method was applied to determine the wt% calcium contents of the different bone types. The semi-quantitative evaluation procedure was derived from Roschger et al. (Roschger et al., 1995) and Zizak et al. (Zizak et al., 2003), where the calcium content was calculated based on the conversion of grey values of the BEI images to mineral volume fraction values. For that purpose, the use of reference materials with known atomic numbers are essential. In this study graphite and magnesium fluoride were chosen as successfully implemented before (Zanghellini et al., 2019).

2.4. Raman spectroscopy

Following SAXS and BEI analysis, Raman measurements were carried out using a confocal Raman microscope (alpha3000 RA, WITec) equipped with a CCD detector. For all experiments, a 633 nm laser with 20 mW power was chosen. Each measurement point that was acquired consisted of 10 accumulations with an integration time of 2 s each. Overview images were collected using a 10x objective with a numerical aperture of 0.25 and a working distance of 11 mm. Raman images were then generated using a 100x objective with a numerical aperture of 0.9 and a working distance of 0.31 mm. The spot size (the collected volumina) on the sample had a diameter of 250 nm and a depth of 800 nm. The spectral resolution was 4.5 cm^{-1}. Spectra were collected in different areas, either healthy or tumorous bone, as shown in the supplementary Figs. S2–S4 (see supplement). 150 spectra were acquired each, in the tumorous region and the normal region of the sclerosing OS samples, and in the tumorous and normal sample of the parosteal OS, respectively, making 600 spectra in total. Data correction and analysis were accomplished with the spectral analysis program Spectragryph (F. Menges "Spectragryph – optical spectroscopy software", version 1.2.16.1, 2022, https://www.effemm2.de/spectragryph/). Background fluorescence was eliminated by a baseline correction. All spectra were peak normalized to the phosphate band at 958 cm^{-1} (Morris and Mandair, 2011). Fig. 1 shows Raman spectra of tumorous and healthy bone and the bands of interest.

Bone-characteristic peaks were determined and relevant peak ratios calculated, which can either be evaluated by using the peak areas or peak intensities (Morris and Mandair, 2011). The most prominent peak intensities in Raman spectra collected from bone originating from mineral and collagen are the ν_1 phosphate band (ν_1 PO_4^{3-} ~ 958 cm^{-1}), the B-type carbonate band (ν_1 CO_3^{2-} ~ 1070 cm^{-1}) and the amide 1 band (~1665 cm^{-1}) (Bi et al., 2013). The amount of mineralization in bone, stated as the mineral-to-matrix ratio, delivers insights in the bone composition and can be calculated by the ratio of the ν_1 phosphate band to the amide 1 band (McCreadie et al., 2006). Bone remodeling, osteoid production and turnover processes can be analyzed trough the carbonate-to-amide 1 and the carbonate-to-phosphate ratio. Furthermore, both parameters, the mineral-to-matrix ratio, and the carbonate-to-matrix ratio, allow to indicate the bone's mechanical properties (Ciubuc et al., 2018).

The inverse full-width-half-maximum (FWHM) of the ν_1 phosphate peak is used to get insights into the mineral crystallinity, in this context meaning an increase in the crystal size and/or atomic ordering and was used in bone before by others (Akkus et al., 2003; Kavukcuoglu et al., 2007; Mandair and Morris, 2015). In bone mineral, the predominant substitution is the B-type carbonate substitution, where CO_3^{2-} is replacing PO_4^{3-}, compared to the A-type substitution where carbonate is substituting OH^- ions. Therefore, the carbonate-to-phosphate ratio typically reflects the carbonation present in the bone samples. Integration areas were chosen in accordance to Huang et al. (Huang et al., 2013) from 930 cm^{-1} to 980 cm^{-1} for ν_1 PO_4^{3-}, from 1050 cm^{-1} to 1100 cm^{-1} for ν_1 CO_3^2 and 1620 cm^{-1} to 1700 cm^{-1} for amide 1.

2.5. Statistical analysis

Statistical analysis to detect differences between healthy bone, tumorous bone tissue and osteosarcoma types was performed using one-way analysis of variance (ANOVA) with post Holm-Bonferroni test to compare all groups and a Kolmogorov-Smirnov test on the tumor and healthy bone tissue sample of each patient. For all tested parameters the ANOVA test showed significant differences. Thus, the asterisk in the plots and tables represent only the results of the two-sample Kolmogorov-Smirnov test within the specimen of the two patients. The significance level was set at $p < 0.05$. Normality of the distribution was tested by visual inspection of histograms of the data.

3. Results

3.1. Structural and composition changes in cancerous bone

Small-angle x-ray scattering (SAXS) data were used to determine the thickness of the mineral particles through the T-parameter as described in the literature (Fratzl et al., 1996; Fratzl et al., 1991; Pabisch et al., 2013). Maps are shown in the supplementary Figs. S5–S8 and

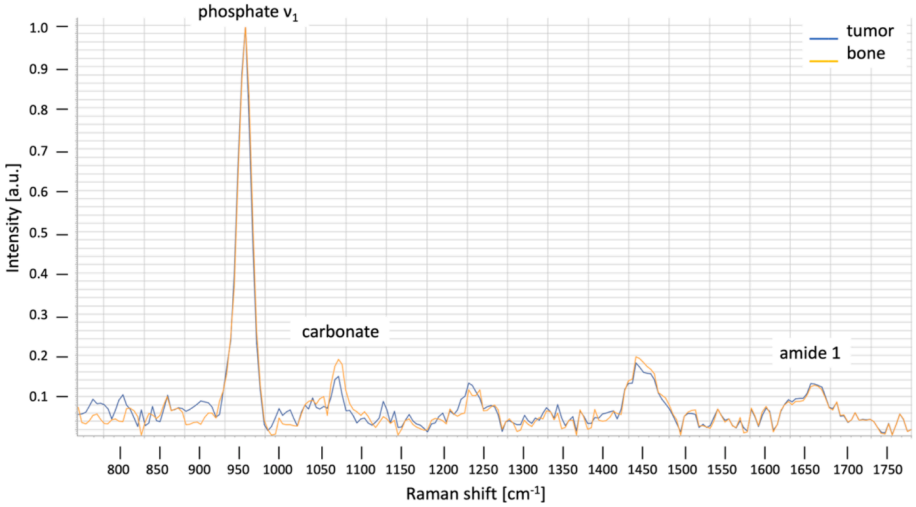

Fig. 1. Raman spectra of healthy and tumorous bone tissue, peaks used for data evaluation are indicated.

histograms in the supplementary Figs. S9–S12 (see supplemental). SAXS data for the sclerosing OS are already published and were taken from (Zanghellini et al., 2019). Arithmetic mean values were calculated in order to average out local variations and to study differences between healthy and tumorous tissue. Due to the large maps, the number of points averaged was in the range of 2–3 millions. Mean T-parameter values in cancerous bone were slightly reduced in the sclerosing and parosteal OS, as compared to normal bone. It should be noted, however, that the T-parameter also varied between the samples of the different patients: T-parameter values for both, N_p and T_p, were almost twice as high as in N_s and T_s, respectively. Such inter-individual differences can never be excluded. Therefore, the comparison of normal and cancerous tissue within one patient is important. Furthermore, the degree of orientation of mineral particles, represented by the ρ-parameter, was deduced from the scattering pattern, as described e.g. in (Rinnerthaler et al., 1999). Assuming parallel arrangement of mineral platelets and the collagen molecules in the collagen-mineral composite (Olszta et al., 2007), this value provides also information on orientation of the collagen fibers. The normal bone tissue samples from both patients showed comparable mean values of the ρ-parameter between each other and with the literature (Li et al., 2010; Zizak et al., 2003), whilst both tumorous bone tissue samples, T_s and T_p, showed clearly reduced mean values of the ρ-parameter i.e., a reduced degree of orientation of collagen-mineral composite in the bone.

In Fig. 2, the morphology of the tumor samples is shown. The sclerosing OS grew inside normal trabecular bone and is distinguished from normal bone by a fuzzy appearance (Fig. 2a, image adapted from (Zanghellini et al., 2019)). By contrast, the parosteal OS tumor sample (T_p) showed a somewhat distorted, but still more compact bone morphology (Fig. 2b). For comparison, images from the normal trabecular bone sample (N_p) from the parosteal OS patient are shown in the supplemental Fig. S1 (supplement). The mineral content was determined by backscattered electron imaging (BEI). The mean and peak calcium content and the mineral volume fraction of bone was calculated by evaluating and converting the grey values of the BEI images in Fig. 2.

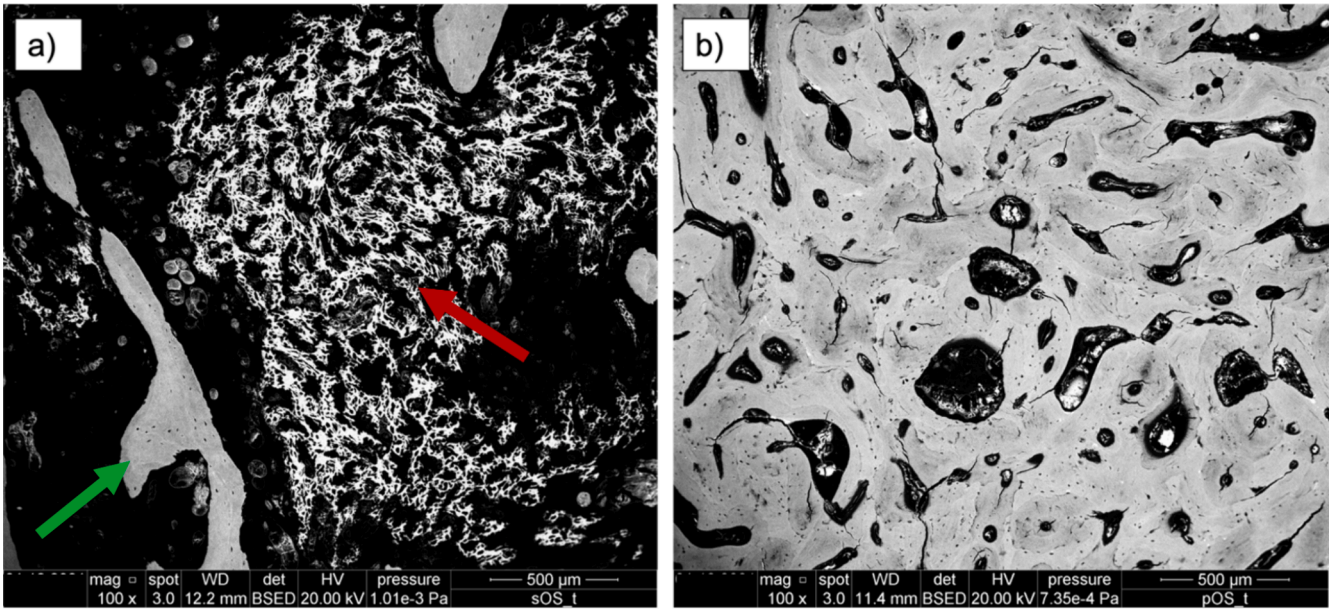

Fig. 2. Backscattered electron image of (a) sclerosing os (red arrow), together with normal bone trabeculae (green arrow), adapted from (Zanghellini et al., 2019) and (b) parosteal OS (tumor tissue only). Due to the Z-contrast, brighter parts are indicating a higher amount of calcium, and thus a higher amount of bone mineral in those areas. (For interpretation of the references to colour in this figure legend, the reader is referred to the web version of this article.)

In Fig. 3, bone mineral density distribution (BMDD) plots according to (Roschger et al., 2008) are shown for sclerosing OS (a) and parosteal OS (b), respectively.

The T_s sample showed higher values of calcium content, and thus a higher mineral content, Φ, compared to N_s, which was also found for other sclerosing osteosarcoma in the literature (Hofstaetter et al., 2013). By contrast, the T_p specimen showed decreased calcium and mineral values compared to N_p (normal bone). All values are summarized in Table 1.

The structure of the bone mineral hydroxyapatite (HAp) was evaluated from the wide-angle x-ray scattering (WAXS) data. For the sclerosing osteosarcoma, this had already been done in a previous study (Zanghellini et al., 2019). There we found a clear shift of the 002 reflection of HAp towards higher q-values for the tumorous bone tissue compared to the healthy tissue parts in the sclerosing OS, corresponding to a reduction of d-spacing of the 002 planes (d002) from 0.3454 nm to 0.3436 nm (Zanghellini et al., 2019). In the present study, we also measured and evaluated d002 for the parosteal OS sample and found that the values in tumorous tissue were significantly ($p < 0.05$) reduced compared to healthy bone tissue (N_p: 0.3441 nm ± 0.0019 nm, T_p: 0.3438 ± 0.0004 nm, number of points averaged per sample: N = 2000), although the differences in the c-axis contraction between healthy and tumorous bone tissue were more pronounced in the sclerosing OS. This means that the c-axis of the bone's HAp crystals are affected by a contraction of the lattice spacing in both tumor samples investigated, but less so in parosteal OS.

3.2. Raman spectra reveal stoichiometric changes

The mineralization in bone was further analyzed by Raman spectroscopy. One parameter of interest was the mineral-to-matrix ratio (MMR) determined from the ratio of the area of the phosphate band at 958 cm^{-1} and the area of the amide 1 band at 1665 cm^{-1}. Fig. 4a) and

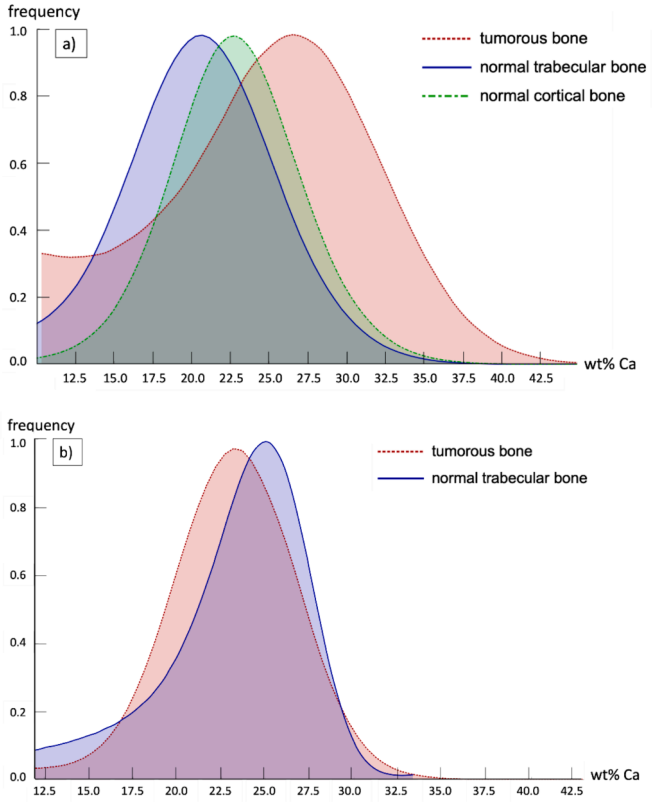

Fig. 3. BMDD plots of (a) sclerosing OS (adapted from (Zanghellini et al., 2019)) and (b) parosteal OS.

Table 1
List of SAXS results (ρ-parameter and T-parameter, upper panel of table) and BEI results (calcium content and mineral volume fraction Φ, lower panel of table) of sclerosing and parosteal OS. Data for the sclerosing OS have already been published and are taken from (Zanghellini et al., 2019). Mean values of the measurement points are shown, alongside with the standard deviation (SD). N is the number of points averaged.

Sample/SAXS	N	T-parameter (nm)	SD (nm)	ρ-parameter	SD
N_p	2.5×10^6	4.497*	0.433	0.476*	0.18
T_p	2.2×10^6	4.402*	0.186	0.343*	0.107
N_s (Zanghellini et al., 2019)	2.9×10^6	2.871*	0.115	0.516*	0.087
T_s (Zanghellini et al., 2019)	2.7×10^6	2.488*	0.28	0.352*	0.136

Sample/BEI	N	Mean Ca content (wt%)	SD (wt %)	Φ (%)
N_p	3.2×10^6	23.44	3.63	38.79
T_p	3.2×10^6	21.76	4.52	34.81
N_s (Zanghellini et al., 2019)	3.2×10^6	22.84	4.408	37.34
T_s (Zanghellini et al., 2019)	3.2×10^6	24.63	6.175	41.79

4b) shows the MMR for healthy and tumorous bone tissue for both OS types. The MMR was reduced in T_p by 24.54 % ($p < 0.05$), while the T_s increased by 65 % ($p < 0.05$) compared to N_s, suggesting a higher mineralization in the sclerosing osteosarcoma compared to the healthy bone, which is also in line with the higher calcium content in sclerosing OS.

The bone mineral crystallinity was analyzed by the inverse FWHM of the phosphate band at 958 cm^{-1}. A narrower band suggests a higher degree of crystallinity of the bone mineral. Fig. 4c) and 4d) shows the evaluated data for all samples. For both bone cancer types values significantly dropped, the T_s by 1.55 % ($p < 0.05$) and the T_p by 1.95 % ($p < 0.05$) compared to the healthy reference samples.

The carbonate-to-phosphate ratio calculated by the integrated intensity areas of the phosphate band at 958 cm^{-1} and the carbonate band at 1070 cm^{-1} reflects the carbonate substitution process in bone. In the T_s sample, the carbonate to phosphate ratio was reduced by 30.76 % ($p < 0.05$) compared to N_s (Fig. 4f). The difference between the T_p and N_p was marginal (Fig. 4e), the ratio decreased by 0.84 % in the tumorous bone sample, which is statistically not significant ($p = 0.552$).

The carbonate-to-amide 1 ratio is related to both, the carbonate substitution in mineral and the mineral to matrix ratio. The sclerosing OS carbonate-to-amide 1 ratio (Fig. 4h) increased by 14.8 % ($p < 0.05$) compared to the normal bone, while in parosteal OS the carbonate-to-amide 1 ratio (Fig. 4g decreased by 18.2 % ($p < 0.05$). Values for all evaluated Raman parameters can be found in Table 2.

4. Discussion

The multimodal approach in this study allowed us to analyze and correlate the ultrastructural and composition differences but also commonalities of two different osteosarcomas collected from two different individuals, and provides a structural assessment on various hierarchical levels of the cancer formation. Table 3 shows an overview of all evaluated parameters of the two different tumor samples in comparison.

SAXS measurements revealed quantitative differences in the degree of orientation of the mineral platelets, and thus the collagen fibers in both cancer-affected bone samples, whilst the normal bone tissue samples revealed values similar to what was found before by others (Fratzl, 1994; Liu et al., 2010). The thickness of the mineral particles (T-

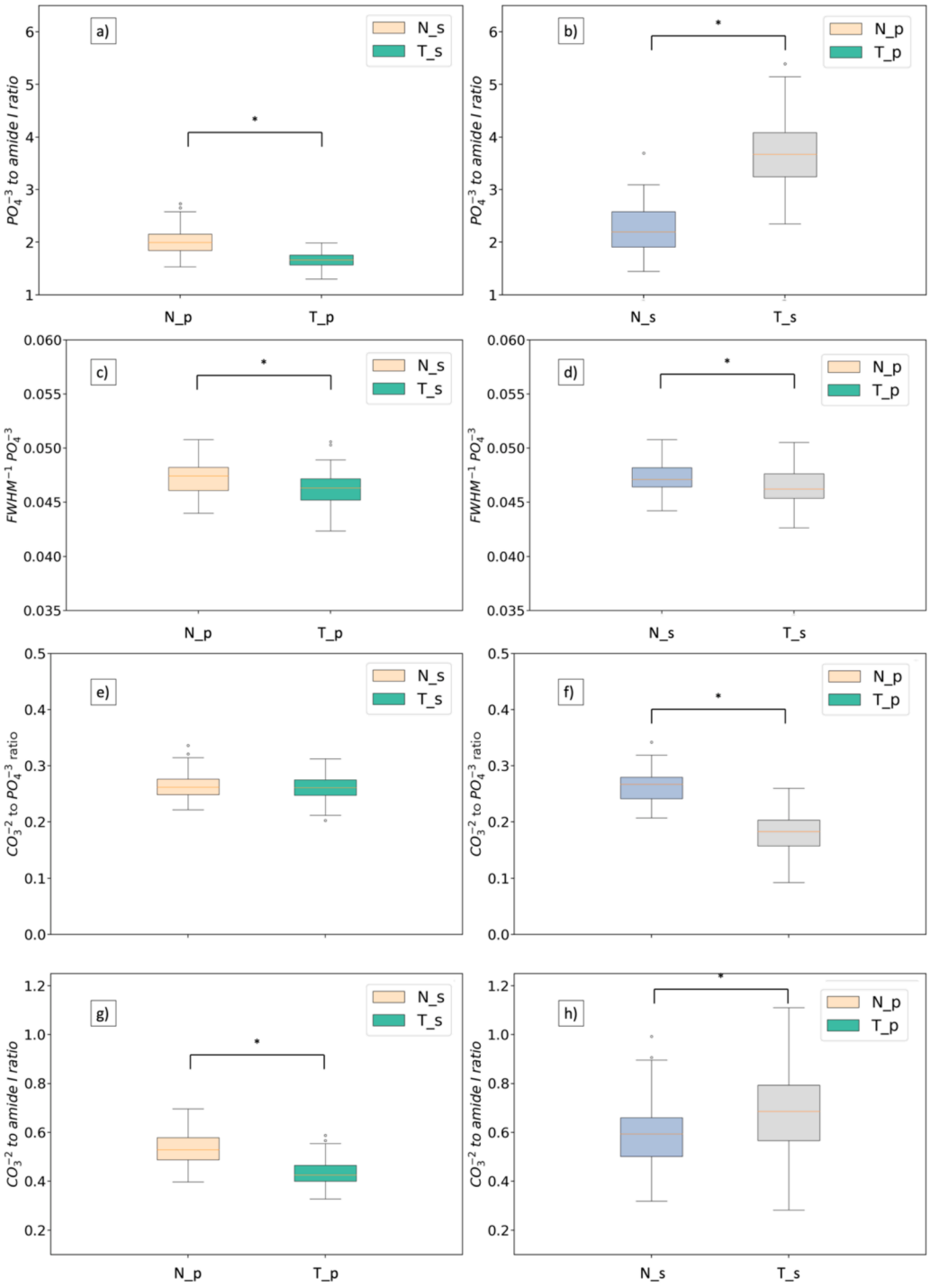

Fig. 4. Mineral-to-matrix ratio calculated from phosphate-to-amide 1 ratio (a) in parosteal OS and (b) sclerosing OS; Reciprocal full-width-half-maximum of the phosphate peak values indicating degree crystallinity of (c) parosteal OS and (d) sclerosing OS; carbonate-to-phosphate ratios describing the carbonate substitution in bone for (e) parosteal OS and (f) sclerosing OS; carbonate-to-amide 1 ratios for (g) parosteal and (h) sclerosing OS.

parameter), however, differed between the two OS types. Whilst the T_s revealed a clear reduction of the mineral particle size compared to healthy bone, the values for the T_p were only reduced by a margin compared to N_p. The degree of orientation of the mineral particles was reduced for both tumor samples in a similar way by 31.8 % and 27.9 %, respectively. The normal bone regions showed values close to 0.5 and fit well to those values (mean 0.5) that are found in literature (Li et al., 2010; Zizak et al., 2003). In mice suffering from bone metastasis of breast cancer, He et al. found reduced T- and ρ-parameter in the metastatic regions compared to healthy parts (He et al., 2017). The reduced mineral platelet thickness could be interpreted as the occurrence of immature HAp crystals in the affected areas.

WAXS data from the sclerosing (Zanghellini et al., 2019) and parosteal OS revealed a contraction of the c-axis of HAp crystals in tumorous regions. Although the differences were smaller in numbers than the instrument resolution determined by standard samples in both cases, it should be noted that the instrument resolution is given as the peak width, while shifts of the peak centroid can be detected with much higher accuracy.

Compared to synthetic HAp, the mineral crystals in bone differ due to

Table 2
Summary of Raman results in tumorous and normal bone. Averaged results from 150 spectra collected in each area (N_p, T_p, N_s and T_s, respectively) are presented.

sample	PO_4^{3-}/amide 1, mean (SD)	$FWHM^{-1}$ PO_4^{3-}, mean (SD)	CO_3^{2-}/PO_4^{3-}, mean (SD)	CO_3^{2-}/amide 1, mean (SD)
N_p	2.20 (0.25)	0.0472 (0.0015)	0.265 (0.023)	0.533 (0.067)
T_p	1.66 (0.14)	0.0463 (0.0016)	0.262 (0.022)	0.436 (0.052)
N_s	2.26 (0.46)	0.0472 (0.0015)	0.264 (0.029)	0.596 (0.129)
T_s	3.73 (0.69)	0.0465 (0.0017)	0.183 (0.036)	0.684 (0.186)

Table 3
Overview of evaluated parameters. Arrows denote an increase (yellow arrow up) or decrease (blue arrow down) of the specific parameter as compared to normal bone (* significant difference). Values that were almost identical with healthy bone are denoted by a white horizontal arrow.

Parameter	Sclerosing OS	Parosteal OS
T-parameter	↓ −13.4 %*	↓ −2.2 %*
ρ-parameter	↓ −31.8 %*	↓ −27.9 %*
d-spacing	↓ −0.5 %*	↓ −0.1 %*
MMR	↑ +65 %*	↓ −24.5 %*
Crystallinity	↓ −1.55 %*	↓ −1.95 %*
Carbonate/phosphate	↓ −30.8%*	→ −0.8 %
Carbonate/amide	↑ +14.8 %*	↓ −18.2 %*

ion substitution. The most abundant ion is carbonate, either substituting OH^- (classified A-type) or PO_4^{-3} (classified B-type). Due to the different ionic radii, an A-type substitution leads to a shrinkage of the c-axis of HAp, whilst a B-type substitution results in an expansion of the c-axis (Kovaleva et al., 2008). It is well documented in literature that the predominant substitution site in bone is the B-type carbonation (Morris et al., 2002; Rey et al., 1989). Evaluation of the carbonate-to-phosphate ratio of the integrated Raman peaks allows to analyze the carbonate substitution type in the different bone areas. The tumorous parts T_s of the sclerosing OS showed a significantly lower ($p < 0.05$) mean value of the carbonate-to-phosphate ratio ($CO_3^{-2}/PO_4^{-3} = 0.183 \pm 0.036$), compared to N_s ($CO_3^{-2}/PO_4^{-3} = 0.264 \pm 0.029$). Thus, in cancerous parts a reduced level of carbonate is present. Given the decrease in the carbonate-to-phosphate ratio in the tumor and the observed prevalence of B-type carbonation in normal bone, the c-axis shrinkage in cancerous parts is compatible with a reduced B-type substitution in the sclerosing OS, rather than an increased A-type substitution. Nevertheless, also other ion substitutions are possible, since a variety of trace elements are present in bone. For example, Mg an Sr are known for their ability to substitute Ca in HAp, which was found to result in a lattice contraction in case of Mg due to the smaller ionic radius (Laurencin et al., 2011) and a lattice expansion for Sr (Bigi et al., 2007). In sclerosing osteosarcoma, elevated levels of Zn have been reported (Rauwolf et al., 2017). It has been shown that Zn may partially substitute Ca ions in HAp, resulting in a decrease of the lattice parameters at low concentrations and a slight increase at higher concentrations (Ren et al., 2009). Since trace elements were not investigated in the present study, further experiments are needed to clarify further potential effects of trace elements on the crystal structure in addition to carbonation. Concerning the parosteal OS, carbonate-to-phosphate ratios for both, N_p and T_p, did not differ significantly and were almost identical with 0.264 (±0.023) and 0.262 (±0.022), respectively. The d-spacing values in c-direction calculated from XRD measurements differed only by a margin, nevertheless differences were significant, indicating that the XRD measurements are more sensitive to small changes or may reflect other ion substitutions in addition to carbonation. Since carbonation in bone is a process that takes time, decreased carbonate levels (as observed via the decreased CO_3^{-2}/PO_4^{-3} ratio) have been associated with a higher bone turnover rate in the literature (Isaksson et al., 2010; Turunen et al., 2013).

The inverse of the FWHM of the ν_1 phosphate peak describes the mineral crystallinity. It correlates with the stoichiometric perfection and the size of the HAp crystal but also reflects its maturity (Bi et al., 2013; Yerramshetty and Akkus, 2008). In this study a significant decrease ($p < 0.05$) in the 1/FWHM value in both, T_p and T_s, was found compared to the corresponding healthy bone samples. The reduction of crystallinity in the sclerosing OS can be explained by the increased B-type substitutions (Bi et al., 2013) compared to healthy bone, while the observed changes of crystallinity in the parosteal OS could not be explained by the mostly unchanged CO_3^{-2}/PO_4^{-3} ratio. Nevertheless, it was stated in the literature that the mineral crystallinity can remain unchanged throughout such stoichiometric changes (Morris and Mandair, 2011). To analyze the bone mineral properties further, additional parameters were evaluated: the mineral-to-matrix ratio (phosphate-to-amide 1 ratio) and the carbonate-to-amide 1 ratio were both increased in sclerosing OS. Semi-quantitative backscattered electron imaging revealed an increased calcium level (+7.84 %) in the tumorous tissue of the sclerosing OS compared to the N_s sample, while in the parosteal OS a slight reduction (−7.17 %) of calcium content was found compared to the N_p sample. These findings indicate different features of the two different osteosarcomas studied here that are compatible with general properties of the involved OS types: higher mineralization i.e., higher calcium content, are typical for sclerosing OS (Hofstaetter et al., 2013; Klein and Siegal, 2006) and further, osteoblastic OS types (like the sclerosing OS) are characterized as high-grade tumors with high growing rates i.e., high turnover rates. By contrast, parosteal OS is characterized as a low-grade tumor with slow growing rates (Hang and Chen, 2014), which is in line with lower turnover rates.

We are aware that our study also faces some limitations, because of the fact that only one sample of each OS type could be studied. This is due to the relatively rare occurrence of OS in general, which generates limits for the availability of samples. Nevertheless, we tried to obtain valid results within those limits by measuring a large number of data points, thus averaging out local variations.

Even though the trends we observe in the two studied OS samples reflect the expression of the disease in two individuals only, we speculate that some of them may be specific to the tumor type. It is, therefore, of interest to consider how the investigated parameters are expressed in other tumor types studied in the literature. In Table 4, a summary of our results is presented together with a comparison of observed tumor affected parameters with those found in the literature for different tumor types.

Bi et al. found for prostate cancer bone metastases of different patients, which were either osteolytic or osteoblastic, distinct differences between the two types: a decreased carbonate-to-phosphate ratio in the osteoblastic and an increased value in the osteolytic samples compared to normal bone. In both, the inverse FWHM of the phosphate peak was smaller compared to normal bone, the mineral-to-matrix ratio was reduced in the osteolytic and higher in the osteoblastic sample compared to the control sample (Bi et al., 2010). In mixed osteoblastic/osteolytic prostate cancer metastases in mice, an increased CO_3^{-2}/PO_4^{-3} ratio, a reduced mineral-to-matrix ratio and a decreased value of crystallinity in the tumor-bearing bones was found compared to the control group (Bi et al., 2013). An increase of carbonate substitution, the mineral-to-matrix ratio and the mineral crystallinity was also found in osteolytic breast cancer metastases in bone. This contrasts with the typical behavior of such lesions. Ding et al. explained this with a possible tissue compensatory response to the bone loss caused by the cancer (Ding et al., 2014). He et al. found increased mineral-to-matrix ratios, as well as a reduction in the mineral crystallinity in combination with a reduced T- and ρ-parameter in osteolytic breast cancer metastases in mice (He et al., 2017). Khalid et al. investigated in-vitro the mineral quality in Staphylococcus aureus – which causes osteomyelitis – in infected human bone samples. They found a great increase in the carbonate-to-

Table 4
Summary of our results and comparison of observed tumor affected parameters with those found in the literature for different tumor types. Arrows denote an increase (yellow arrow up) or decrease (blue arrow down) or almost identical values (horizontal white arrow) of the specific parameter as compared to normal bone.

Samples in this study	T-param.	ρ-param.	carb./phos.	carb./amid.	MMR	Crystallinity
Sclerosing osteosarcoma	↓	↓	↓	↑	↑	↓
Parosteal osteosarcoma	↓	↓	→	↓	↓	↓

Disease type, from literature	T-param.	ρ-param.	carb./phos.	carb./amid.	MMR	Crystallinity	Ref.
Osteolytic metastases, breast cancer	↓	↓	/	/	↑	↓	(He et al., 2017)
Osteoblastic metastases, prostate cancer	/	/	↓	/	↑	↓	(Bi et al., 2010)
Osteolytic metastases, prostate cancer	/	/	↑	/	↓	↓	(Bi et al., 2010)
Osteolytic metastases, breast cancer	/	/	↑	/	↑	↑	(Ding et al., 2014)
Staphylococcus aureus	/	/	↑	↓	↓	↓	(Khalid et al., 2018)

phosphate ratio in the affected samples and related this to an enhanced B-type substitution due to the bacterial infection. Furthermore, a reduction in crystallinity in the infected bone samples was detected (Khalid et al., 2018). All these studies including our findings (except Ding et al. due to possible tissue compensatory response (Ding et al., 2014)) found a reduction in the mineral crystallinity when affected from disease.

In the present study, we found similar structural changes in both OS samples: reduced mineral particle thickness and a reduced degree of orientation of collagen-mineral composite in the affected areas, but also a mineral lattice contraction compatible with a reduced B-type carbonation in the sclerosing OS sample, which could be explained by the substantially increased bone mineral formation processes.

Furthermore, the sclerosing OS sample studied here showed clear characteristics of osteoblastic dominant lesions: lower carbonate-to-phosphate ratio, increased turnover rates and an enhanced mineral-to-matrix ratio. However, the parosteal OS sample revealed characteristics of osteolytic dominant lesions: a decrease in mineral-to-matrix ratio, but no significant difference in the carbonate-to-phosphate ratio compared to healthy bone, suggesting a similar turnover rate.

Concerning early diagnostic measurements, studies have found that the carbonate level in bone could be a good indicator for malignancy in breast cancer: it was found that benign lesions had higher carbonate levels than malignant ones (Haka et al., 2002; Kerssens et al., 2010). Here we found a reduced carbonate level only for the sclerosing OS sample, whilst a contraction of the c-axis in the tumorous areas compared to healthy bone could be proven for both OS samples. Due to the fact, that the crystallinity and the c-axis was reduced in both, parosteal and sclerosing samples, we speculate that the crystal lattice contraction (even though much less pronounced in parosteal OS) and the reduced mineral crystallinity could be typical features for osteosarcomas, potentially independent of the subtype. It is interesting to study if they can also serve as general indicators of malignant calcified lesions.

5. Conclusion

In this study we investigated stoichiometric and ultrastructural changes in two osteosarcoma samples of different subtypes, a sclerosing and a parosteal OS by a multimodal approach. SAXS measurements on the parosteal OS showed a clear reduction of the mineral particle thickness and the degree of orientation of the collagen-mineral composite, while WAXS measurements demonstrated a contraction of the c-axis in the tumorous areas. These changes were in line with those previously found in a sclerosing OS (Zanghellini et al., 2019). By contrast, BEI results showed a marked decrease of calcium content in the parosteal OS, which is in contrast to the increased calcium level in the sclerosing OS (Zanghellini et al., 2019). Raman spectroscopy measurements on both tumor samples revealed marked differences in the carbonate substitution, indicative of a different turnover rate. These findings can help to understand the ultrastructure and properties of ostesarcomas. Furthermore, if cancer specific mineral crystal changes can be identified, they may be used in the future for highly sensitive ex-vivo analysis or the development of new in-vivo screening methods based on e.g., spatially offset Raman spectroscopy to study cancer-associated changes in bone.

CRediT authorship contribution statement

Benjamin Zanghellini: Writing – original draft, Methodology, Investigation, Conceptualization. **Nicole Zechmann:** Investigation. **Dieter Baurecht:** Writing – review & editing, Supervision, Methodology. **Tilman A. Grünewald:** Writing – review & editing, Methodology, Investigation, Conceptualization. **Manfred Burghammer:** Writing – review & editing, Methodology. **Bernadette Liegl-Atzwanger:** Writing – review & editing, Conceptualization. **Andreas Leithner:** Writing – review & editing, Conceptualization. **Anton Davydok:** Writing – review & editing, Methodology. **Helga Lichtenegger:** Writing – review & editing, Supervision, Funding acquisition, Conceptualization.

Declaration of competing interest

The authors declare that they have no known competing financial interests or personal relationships that could have appeared to influence the work reported in this paper.

Data availability

Data will be made available on request.

Acknowledgements

We would like to thank Thomas Bretschneider for his encouraging assistance and contribution prior to and during the PETRAIII/P03 beam time.

We acknowledge the European Synchrotron Radiation Facility (ESRF) for provision of beam time on ID13 and we would like to thank the beamline staff for assistance. We acknowledge DESY (Hamburg, Germany), a member of the Helmholtz Association HGF, for the

provision of experimental facilities. Parts of this research were carried out at beamline PETRAIII/P03 and we would like to thank the beamline staff for assistance during the experiment.

This work was supported by the Austrian Science Funds FWF [grant no. I 4409-B].

Appendix A. Supplementary material

Supplementary data to this article can be found online at https://doi.org/10.1016/j.jsb.2024.108106.

References

Akkus, O., Polyakova-Akkus, A., Adar, F., Schaffler, M.B., 2003. Aging of microstructural compartments in human compact bone. J. Bone Miner. Res. 18, 1012–1019.
Almer, J.D., Stock, S.R., 2005. Internal strains and stresses measured in cortical bone via high-energy X-ray diffraction. J. Struct. Biol. 152, 14–27.
Baumhoer, D., 2018. Pathogenese und genetischer Hintergrund des Osteosarkoms. Pathologe 39, 139–145.
Bi, X., Patil, C., Morrissey, C., Roudier, M., Mahadevan-Jansen, A., Nyman, J., 2010. Characterization of bone quality in prostate cancer bone metastases using Raman spectroscopy SPIE.
Bi, X., Sterling, J.A., Merkel, A.R., Perrien, D.S., Nyman, J.S., Mahadevan-Jansen, A., 2013. Prostate cancer metastases alter bone mineral and matrix composition independent of effects on bone architecture in mice–a quantitative study using microCT and Raman spectroscopy. Bone 56, 454–460.
Bigi, A., Boanini, E., Capuccini, C., Gazzano, M., 2007. Strontium-substituted hydroxyapatite nanocrystals. Inorg. Chim. Acta 360, 1009–1016.
Cheng, G., Zhang, Y., Yin, H., Ruan, Y., Sun, Y., Lin, K., 2019. Effects of strontium substitution on the structural distortion of hydroxyapatite by rietveld refinement and Raman Spectroscopy. Ceram. Int. 45, 11073–11078.
Ciubuc, J.D., Manciu, M., Maran, A., Yaszemski, M.J., Sundin, E.M., Bennet, K.E., Manciu, F.S., 2018. Raman spectroscopic and microscopic analysis for monitoring renal osteodystrophy signatures. Biosensors (Basel) 8.
Davies, E., Müller, K.H., Wong, W.C., Pickard, C.J., Reid, D.G., Skepper, J.N., Duer, M.J., 2014. Citrate bridges between mineral platelets in bone. Proc. Natl. Acad. Sci. 111, E1354–E1363.
Ding, H., Nyman, J.S., Sterling, J.A., Perrien, D.S., Mahadevan-Jansen, A., Bi, X., 2014. Development of Raman spectral markers to assess metastatic bone in breast cancer. J. Biomed. Opt. 19, 111606.
Dorozhkin, S.V., Epple, M., 2002. Die biologische und medizinische Bedeutung von Calciumphosphaten. Angew. Chem. 114, 3260–3277.
Fratzl, P., 1994. Statistical-model of the habit and arrangement of mineral crystals in the collagen of bone. J. Stat. Phys. 77, 125–143.
Fratzl, P., Fratzl-Zelman, N., Klaushofer, K., Vogl, G., Koller, K., 1991. Nucleation and growth of mineral crystals in bone studied by small-angle X-ray scattering. Calcif. Tissue Int. 48, 407–413.
Fratzl, P., Schreiber, S., Klaushofer, K., 1996. Bone mineralization as studied by small-angle x-ray scattering. Connect. Tissue Res. 34, 247–254.
Grandfield, K., Vuong, V., Schwarcz, H.P., 2018. Ultrastructure of bone: hierarchical features from nanometer to micrometer scale revealed in focused ion beam sections in the TEM. Calcif. Tissue Int. 103, 606–616.
Grünewald, T.A., Ogier, A., Akbarzadeh, J., Meischel, M., Peterlik, H., Löffler, J.F., Stanzl-Tschegg, S., Weinberg, A.M., Lichtenegger, H.C., 2016a. Reaction of bone nanostructure towards a biodegrading Magnesium WZ21 implant – a scanning small angle X-ray scattering time-study. Acta Biomater. 31, 448–457.
Grünewald, T.A., Rennhofer, H., Hesse, B., Burghammer, M., Stanzl-Tschegg, S., Cotte, M., Löffler, J.F., Weinberg, A.M., Lichtenegger, H.C., 2016b. Magnesium from bioresorbable implants: distribution and impact on the nano- and mineral structure of bone. Biomaterials 76, 250–260.
Grünewald, T.A., Liebi, M., Wittig, N.K., Johannes, A., Sikjaer, T., Rejnmark, L., Gao, Z., Rosenthal, M., Guizar-Sicairos, M., Birkedal, H., Burghammer, M., 2020. Mapping the 3D orientation of nanocrystals and nanostructures in human bone: indications of novel structural features. Sci. Adv. 6, eaba4171.
Gupta, H.S., Seto, J., Wagermaier, W., Zaslansky, P., Boesecke, P., Fratzl, P., 2006. Cooperative deformation of mineral and collagen in bone at the nanoscale. Proc. Natl. Acad. Sci. 103, 17741–17746.
Haka, A.S., Shafer-Peltier, K.E., Fitzmaurice, M., Crowe, J., Dasari, R.R., Feld, M.S., 2002. Identifying microcalcifications in benign and malignant breast lesions by probing differences in their chemical composition using Raman spectroscopy. Cancer Res. 62, 5375–5380.
Hang, J.F., Chen, P.C., 2014. Parosteal osteosarcoma. Arch. Pathol. Lab. Med. 138, 694–699.
He, F., Chiou, A.E., Loh, H.C., Lynch, M., Seo, B.R., Song, Y.H., Lee, M.J., Hoerth, R., Bortel, E.L., Willie, B.M., Duda, G.N., Estroff, L.A., Masic, A., Wagermaier, W., Fratzl, P., Fischbach, C., 2017. Multiscale characterization of the mineral phase at skeletal sites of breast cancer metastasis. PNAS 114, 10542–10547.
Hofstaetter, J.G., Roschger, A., Puchner, S.E., Dominkus, M., Sulzbacher, I., Windhager, R., Klaushofer, K., Roschger, P., 2013. Altered matrix mineralization in a case of a sclerosing osteosarcoma. Bone 53, 409–413.
Huang, H., Feng, S.Y., Chen, W.W., Yu, Y., Lin, D., Chen, R., 2013. Study on fracture healing with small-splint-fixation therapy by near-infrared Raman spectroscopy. J. Spectrosc. 2013.
Imbert, L., Auregan, J.C., Pernelle, K., Hoc, T., 2014. Mechanical and mineral properties of osteogenesis imperfecta human bones at the tissue level. Bone 65, 18–24.
Isaksson, H., Turunen, M.J., Rieppo, L., Saarakkala, S., Tamminen, I.S., Rieppo, J., Kröger, H., Jurvelin, J.S., 2010. Infrared spectroscopy indicates altered bone turnover and remodeling activity in renal osteodystrophy. J. Bone Miner. Res. 25, 1360–1366.
Kansara, M., Thomas, D.M., 2007. Molecular pathogenesis of osteosarcoma. DNA Cell Biol. 26, 1–18.
Karunaratne, A., Davis, G.R., Hiller, J., Esapa, C.T., Terrill, N.J., Brown, S.D.M., Cox, R. D., Thakker, R.V., Gupta, H.S., 2012. Hypophosphatemic rickets is associated with disruption of mineral orientation at the nanoscale in the flat scapula bones of rachitic mice with development. Bone 51, 553–562.
Kavukcuoglu, N.B., Arteaga-Solis, E., Lee-Arteaga, S., Ramirez, F., Mann, A.B., 2007. Nanomechanics and Raman spectroscopy of fibrillin 2 knock-out mouse bones. J. Mater. Sci. 42, 8788–8794.
Kerssens, M.M., Matousek, P., Rogers, K., Stone, N., 2010. Towards a safe non-invasive method for evaluating the carbonate substitution levels of hydroxyapatite (HAP) in micro-calcifications found in breast tissue. Analyst 135, 3156–3161.
Khalid, M., Bora, T., Ghaithi, A.A., Thukral, S., Dutta, J., 2018. Raman spectroscopy detects changes in bone mineral quality and collagen cross-linkage in Staphylococcus infected human bone. Sci. Rep. 8, 9417.
Kim, G., Cole, J.H., Boskey, A.L., Baker, S.P., van der Meulen, M.C., 2014. Reduced tissue-level stiffness and mineralization in osteoporotic cancellous bone. Calcif. Tissue Int. 95, 125–131.
Klein, M.J., Siegal, G.P., 2006. Osteosarcoma: anatomic and histologic variants. Am. J. Clin. Pathol. 125, 555–581.
Kovaleva, E.S., Shabanov, M.P., Putlayev, V.I., Filippov, Y.Y., Tretyakov, Y.D., Ivanov, V. K., 2008. Carbonated hydroxyapatite nanopowders for preparation of bioresorbable materials. Materialwiss Werkst 39, 822–829.
Lala, S., Ghosh, M., Das, P.K., Das, D., Kar, T., Pradhan, S.K., 2016. Magnesium substitution in carbonated hydroxyapatite: Structural and microstructural characterization by Rietveld's refinement. Mater. Chem. Phys. 170, 319–329.
Launey, M.E., Buehler, M.J., Ritchie, R.O., 2010. On the mechanistic origins of toughness in bone. Annu. Rev. Mater. Res. 40, 25–53.
Laurencin, D., Almora-Barrios, N., de Leeuw, N.H., Gervais, C., Bonhomme, C., Mauri, F., Chrzanowski, W., Knowles, J.C., Newport, R.J., Wong, A., Gan, Z., Smith, M.E., 2011. Magnesium incorporation into hydroxyapatite. Biomaterials 32, 1826–1837.
LeGeros, R.Z., Trautz, O.R., Klein, E., LeGeros, J.P., 1969. Two types of carbonate substitution in the apatite structure. Experientia 25, 5–7.
Li, C.H., Paris, O., Siegel, S., Roschger, P., Paschalis, E.P., Klaushofer, K., Fratzl, P., 2010. Strontium is incorporated into mineral crystals only in newly formed bone during strontium ranelate treatment. J. Bone Miner. Res. 25, 968–975.
Liu, Y., Manjubala, I., Schell, H., Epari, D.R., Roschger, P., Duda, G.N., Fratzl, P., 2010. Size and habit of mineral particles in bone and mineralized callus during bone healing in sheep. J. Bone Miner. Res. 25, 2029–2038.
Lokau, J., 2020. Die Rolle von Interleukin-11 beim Osteosarkom, pp. 163, Vol. 41.
Lowenstam, H.A., Weiner, S., 1989. On Biomineralization. Oxford University Press, New York Oxford.
Madupalli, H., Pavan, B., Tecklenburg, M.M.J., 2017. Carbonate substitution in the mineral component of bone: discriminating the structural changes, simultaneously imposed by carbonate in A and B sites of apatite. J. Solid State Chem. 255, 27–35.
Mandair, G.S., Morris, M.D., 2015. Contributions of Raman spectroscopy to the understanding of bone strength. Bonekey Rep. 4, 620.
McCreadie, B.R., Morris, M.D., Chen, T.C., Sudhaker Rao, D., Finney, W.F., Widjaja, E., Goldstein, S.A., 2006. Bone tissue compositional differences in women with and without osteoporotic fracture. Bone 39, 1190–1195.
McKee, M.D., Buss, D.J., Reznikov, N., 2022. Mineral tessellation in bone and the stenciling principle for extracellular matrix mineralization. J. Struct. Biol. 214, 107823.
Morris, M., Stewart, S., Tarnowski, C., Shea, D., Franceschi, R., Wang, D., Ignelzi, M., Wang, W., Keller, E., Lin, D.-L., Goldstein, S., Taboas, J., 2002. Early mineralization of normal and pathologic calvaria as revealed by Raman spectroscopy SPIE.
Morris, M.D., Mandair, G.S., 2011. Raman assessment of bone quality. Clin. Orthop. Relat. Res. 469, 2160–2169.
Mottaghitalab, F., Hosseinkhani, H., Shokrgozar, M.A., Mao, C., Yang, M., Farokhi, M., 2015. Silk as a potential candidate for bone tissue engineering. J. Control. Release 215, 112–128.
Olszta, M.J., Cheng, X.G., Jee, S.S., Kumar, R., Kim, Y.Y., Kaufman, M.J., Douglas, E.P., Gower, L.B., 2007. Bone structure and formation: a new perspective. Mater. Sci. Eng. R-Rep. 58, 77–116.
Pabisch, S., Wagermaier, W., Zander, T., Li, C., Fratzl, P., 2013. Imaging the nanostructure of bone and dentin through small- and wide-angle X-ray scattering. Methods Enzymol. 532, 391–413.
Posner, A.S., 1969. Crystal chemistry of bone mineral. Physiol. Rev. 49, 760–792.
Rauwolf, M., Pemmer, B., Roschger, A., Turyanskaya, A., Smolek, S., Maderitsch, A., Hischenhuber, P., Foelser, M., Simon, R., Lang, S., Puchner, S.E., Windhager, R., Klaushofer, K., Wobrauschek, P., Hofstaetter, J.G., Roschger, P., Streli, C., 2017. Increased zinc accumulation in mineralized osteosarcoma tissue measured by confocal synchrotron radiation micro X-ray fluorescence analysis. X-ray Spectrom. 46, 56–62.
Ren, F., Xin, R., Ge, X., Leng, Y., 2009. Characterization and structural analysis of zinc-substituted hydroxyapatites. Acta Biomater. 5, 3141–3149.

Rey, C., Collins, B., Goehl, T., Dickson, I.R., Glimcher, M.J., 1989. The carbonate environment in bone mineral: a resolution-enhanced Fourier Transform Infrared Spectroscopy Study. Calcif. Tissue Int. 45, 157–164.
Reznikov, N., Shahar, R., Weiner, S., 2014. Bone hierarchical structure in three dimensions. Acta Biomater. 10, 3815–3826.
Reznikov, N., Bilton, M., Lari, L., Stevens, M.M., Kröger, R., 2018. Fractal-like hierarchical organization of bone begins at the nanoscale. Science 360.
Reznikov, N., Hoac, B., Buss, D.J., Addison, W.N., Barros, N.M.T., McKee, M.D., 2020. Biological stenciling of mineralization in the skeleton: local enzymatic removal of inhibitors in the extracellular matrix. Bone 138, 115447.
Rho, J.-Y., Kuhn-Spearing, L., Zioupos, P., 1998. Mechanical properties and the hierarchical structure of bone. Med. Eng. Phys. 20, 92–102.
Rinnerthaler, S., Roschger, P., Jakob, H.F., Nader, A., Klaushofer, K., Fratzl, P., 1999. Scanning small angle X-ray scattering analysis of human bone sections. Calcif. Tissue Int. 64, 422–429.
Rodriguez-Palomo, A., Østergaard, M., Birkedal, H., 2023. Bone hierarchical structure: heterogeneity and uniformity. Adv. Funct. Mater., 2307026
Roschger, P., Plenk Jr., H., Klaushofer, K., Eschberger, J., 1995. A new scanning electron microscopy approach to the quantification of bone mineral distribution: backscattered electron image grey-levels correlated to calcium K alpha-line intensities. Scanning Microsc. 9, 75–86 discussion 86–78.
Roschger, P., Fratzl, P., Eschberger, J., Klaushofer, K., 1998. Validation of quantitative backscattered electron imaging for the measurement of mineral density distribution in human bone biopsies. Bone 23, 319–326.
Roschger, P., Paschalis, E.P., Fratzl, P., Klaushofer, K., 2008. Bone mineralization density distribution in health and disease. Bone 42, 456–466.
Schwarcz, H.P., McNally, E.A., Botton, G.A., 2014. Dark-field transmission electron microscopy of cortical bone reveals details of extrafibrillar crystals. J. Struct. Biol. 188, 240–248.
Tobias, J.S., Hochhauser, D., 2015. Cancer and Its Management. Wiley-Blackwell, Oxford.
Turunen, M.J., Prantner, V., Jurvelin, J.S., Kröger, H., Isaksson, H., 2013. Composition and microarchitecture of human trabecular bone change with age and differ between anatomical locations. Bone 54, 118–125.
Wang, R., Gupta, H.S., 2011. Deformation and fracture mechanisms of bone and nacre. Annu. Rev. Mater. Res. 41, 41–73.
Wang, Y., Von Euw, S., Fernandes, F.M., Cassaignon, S., Selmane, M., Laurent, G., Pehau-Arnaudet, G., Coelho, C., Bonhomme-Coury, L., Giraud-Guille, M.-M., Babonneau, F., Azaïs, T., Nassif, N., 2013. Water-mediated structuring of bone apatite. Nat. Mater. 12, 1144–1153.
Watson, M.L., Avery, J.K., 1954. The development of the hamster lower incisor as observed by electron microscopy. Am. J. Anat. 95, 109–161.
Weiner, S., Wagner, H.D., 1998. THE MATERIAL BONE: structure-mechanical function relations. Annu. Rev. Mater. Sci. 28, 271–298.
Wittig, N.K., Palle, J., Østergaard, M., Frølich, S., Birkbak, M.E., Spiers, K.M., Garrevoet, J., Birkedal, H., 2019. Bone biomineral properties vary across human osteonal bone. ACS Nano 13, 12949–12956.
Yerramshetty, J.S., Akkus, O., 2008. The associations between mineral crystallinity and the mechanical properties of human cortical bone. Bone 42, 476–482.
Zanghellini, B., Grünewald, T.A., Burghammer, M., Rennhofer, H., Liegl-Atzwanger, B., Leithner, A., Lichtenegger, H.C., 2019. High-resolution large-area imaging of nanoscale structure and mineralization of a sclerosing osteosarcoma in human bone. J. Struct. Biol. 207, 56–66.
Zizak, I., Roschger, P., Paris, O., Misof, B.M., Berzlanovich, A., Bernstorff, S., Amenitsch, H., Klaushofer, K., Fratzl, P., 2003. Characteristics of mineral particles in the human bone/cartilage interface. J. Struct. Biol. 141, 208–217.